Journal of Materials Chemistry C

ROYAL SOCIETY OF CHEMISTRY

PAPER

View Article Online
View Journal | View Issue

Cite this: J. Mater. Chem. C, 2024, 12, 3564

The structure of Pd-functionalized UiO-67 during CO_2 hydrogenation†

Alina A. Skorynina, *[a] Andrea Lazzarini, [bc] Dag Kristian Sannes,[b] Elizaveta G. Kozyr, [d] Christian Ahoba-Sam,[b] Silvia Bordiga, [bd] Unni Olsbye *[b] and Aram L. Bugaev *[e]

Received 13th November 2023,
Accepted 30th January 2024

DOI: 10.1039/d3tc04175a

rsc.li/materials-c

The detailed evolution of the local atomic and electronic structure of palladium nanoparticles (NPs) embedded in Zr-based metal–organic frameworks (MOFs) UiO-67 is presented. The samples were employed for CO_2 hydrogenation under different temperatures and at total pressures of 1 or 8 bar. The effects of exposure to the reactive atmosphere and reaction products on the structure of MOFs and Pd NPs were monitored in *operando* mode by simultaneous X-ray diffraction and X-ray absorption spectroscopy measurements. Advanced analysis of large experimental datasets supported by theoretical simulations revealed the formation of mixed carbide and hydride phases of palladium and the adsorption of CO species as reaction intermediates at the surface of Pd NPs under the reaction conditions. According to available information, the observation of the Pd/Zr interface and its association with methanol formation was first obtained in this work for Pd–Zr-MOFs materials.

Introduction

Hydrogenation of CO_2 is an important reaction attracting the attention of researchers over decades and becoming more and more crucial in the context of the green and circular economy. The particular challenge is the ability to reduce the main driver of global warming by converting CO_2 into useful value-added products such as methanol. Prior to this, the hydrogenation of CO_2 to CH_4, also called the Sabatier reaction,[1] was carried out at high temperatures (>300 °C) to promote the kinetics of the reaction. The most popular catalysts for methanation are supported metal systems.[2–7] However, during the hydrogenation reaction in such catalytic systems, the catalyst ages, which is associated with gradual sintering of metal particles and/or adhesion of carbon atoms to nanoparticles (NPs), reducing the number of active sites involved in the reaction.[8–12]

As a solution to the problem of particle sintering, there is a promising way, namely using a stable porous structure as a substrate, inside the pores of which nanoparticles of fixed sizes could be grown. Among all materials possessing such characteristics, we find metal–organic frameworks (MOFs).[13–16] MOFs consist of metal/metal oxide nodes connected by organic linkers into three-dimensional porous crystalline structures. Since these nodes are active by themselves only in a limited number of MOF structures, it is proposed to carry out additional functionalization for catalytic purposes.[17–21] Some of the most promising MOFs are the Zr-based UiO family, displaying exceptional thermal and chemical stability up to the required reaction temperatures.[22–26] Also, in the case of UiO-66/67/68, functionalization has played an important role in enhancing the material potentialities, by insertion of other metals in the inorganic cornerstones[27,28] and by functionalization of linkers with additional metals.[29–33]

Previously, our group has investigated how the CO_2 hydrogenation reaction proceeds on Pt NPs grown inside UiO-67 pores, where the process was monitored by *operando* FT-IR spectroscopy.[34,35] Furthermore, the successful synthesis of palladium NPs inside UiO-67 was studied by X-ray powder diffraction (XRPD) and X-ray absorption spectroscopy (XAS),[36,37] where Pd structural changes were monitored during ethylene hydrogenation.[32,38]

In this work, we have studied structural evolution of Pd@UiO-67 during *operando* carbon dioxide hydrogenation by simultaneous measurements of XRPD, X-ray absorption near edge structure (XANES) and extended X-ray absorption fine

[a] CELLS-ALBA Synchrotron Light Source, Carrer de la Llum, 2, 26, 08290 Cerdanyola del Vallès, Barcelona, Spain. E-mail: askorynina@cells.es
[b] Centre for Materials Science and Nanotechnology, Department of Chemistry, University of Oslo, Sem Saelandsvei 26, 0315 Oslo, Norway. E-mail: unni.olsbye@kjemi.uio.no
[c] Department of Physical and Chemical Sciences, University of L'Aquila, Via Vetoio ("A.C. De Meis" building), 67100 L'Aquila, Italy
[d] Department of Chemistry and NIS Centre, University of Turin, Via Pietro Giuria, 7, 10125 Turin, Italy
[e] SuperXAS beamline, Paul Scherrer Institute, Forschungsstrasse 111, 5232 Villigen, Switzerland. E-mail: aram.bugaev@psi.ch

† Electronic supplementary information (ESI) available: Scheme of the experimental setup, additional XANES and FT-EXAFS spectra, MCR analysis of XANES, atomic models, XRPD data. See DOI: https://doi.org/10.1039/d3tc04175a

structure (EXAFS) spectroscopies. The multivariate curve resolution alternating least squares (MCR-ALS) approach[39–41] was applied to XANES spectra to extract pure species from the whole dataset during the CO_2 hydrogenation reaction under different temperature and pressure conditions. The obtained experimental spectra were complemented by theoretical XANES simulations and density functional theory (DFT)-calculated atomic structures to define surface adsorbed species. XRPD and EXAFS analysis provided values for lattice expansion of the MOFs structure and, respectively, changes in the local environment of Pd atoms. Furthermore, the CO_2 conversion was followed by FT-IR spectroscopy. Finally, the conditions used during XAS and FT-IR measurements were replicated in a catalytic test rig to establish structure/composition – performance correlations for the Pd@UiO-67 catalyst.

Results and discussion

A TEM image of the sample after activation is shown in Fig. 1. The formed Pd NPs, which are regarded to be the active species during CO_2 hydrogenation, can be easily distinguished within the framework. Average size of the particles is *ca.* 2.3 nm (Fig. S1, ESI†),[32] which is in good agreement with the results of EXAFS analysis (*vide infra*). The deviation from the normal distribution (see the inset in Fig. 1) may originate from the co-existence of the particles inside the pores and at the outer surface of MOF crystallites.[21,32,36]

Fig. 2 shows details of *operando* FT-IR spectra of UiO-67-Pd, namely the formate region (2800–2700 cm^{-1}) and CO···Me interaction region (2150–1910 cm^{-1}) collected during CO_2 hydrogenation reaction. Differently from what was observed in our previous research with its Pt-analogue,[35] the Pd catalyst operating at 1 bar total pressure did not develop the typical tiny band of the bidentate formate groups located at 2750 cm^{-1} (Fig. 2a),[35,42] which we identified as the one responsible for methanol production. Indeed, catalytic data collected under the same reaction conditions confirmed such evidence. This behavior was also confirmed at different operating temperatures. Another difference from UiO-67-Pt, is the absence of the interaction of produced CO with Pd NPs that were formed during the activation procedure (Fig. 2b), meaning that CO adsorption is not favorable at such temperature and pressure conditions. However, by varying the total pressure to 8 bar, UiO-67-Pd catalyst started developing the typical bidentate formate spectroscopic feature at 2750 cm^{-1} (Fig. 2c).[35] Such signal is constant throughout the whole catalytic test, similarly to the methanol selectivity that is strictly related to the presence of such species. Furthermore, higher pressure began to favor CO adsorption onto Pd NPs, as visible from gas-phase roto-vibrational signal of CO at 240 °C (red curve, Fig. 2d) and from its typical signal related to linear carbonyl species at 2050 cm^{-1} (brown curve, Fig. 2d).[38,43–45]

The local structures of palladium and zirconium, as well the crystal structure of UiO-67 framework was followed *in situ* starting from the activation of as-prepared UiO-67-Pd under various conditions. Fitting of the EXAFS data collected under each of the experimental conditions provided the evolution of

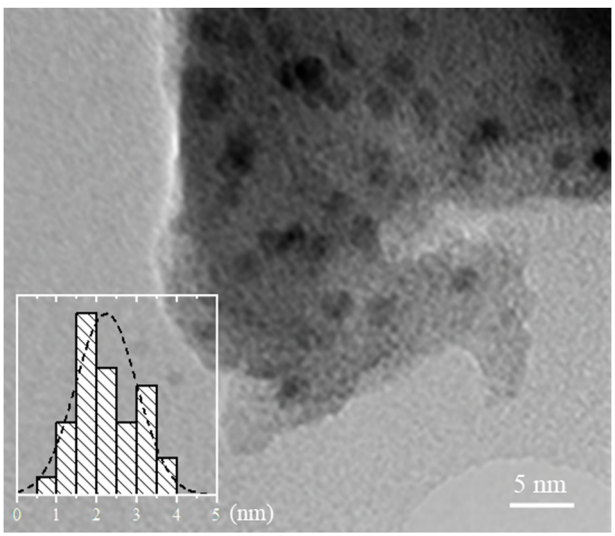

Fig. 1 TEM image of the UiO-67-Pd sample after activation. Size distribution analysis shown in the inset was performed by counting 240 particles from different images of the sample.

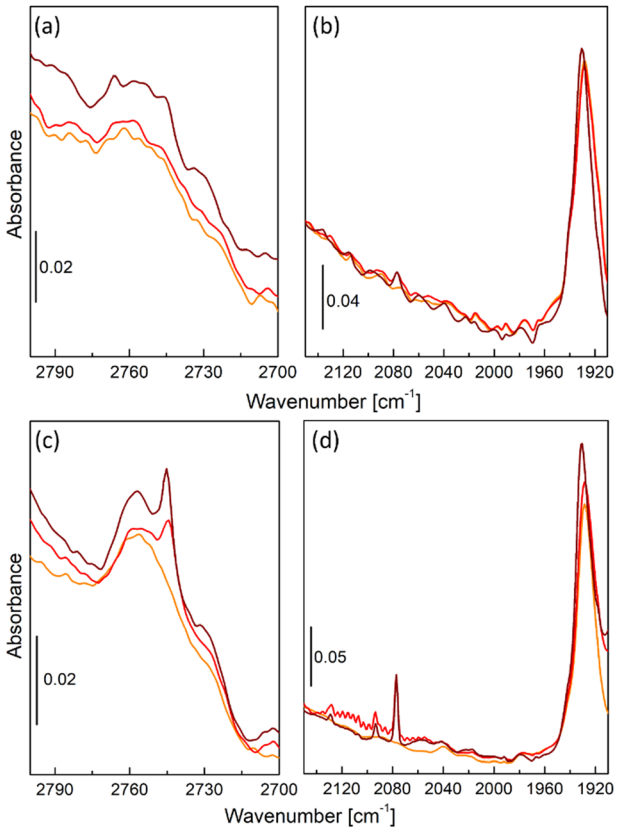

Fig. 2 FT-IR spectra in the formate region (parts (a) and (c)) and CO···Me interaction region (parts (b) and (d)) of UiO-67-Pd in *operando* CO_2 hydrogenation conditions under different total pressure, namely 1 bar (parts (a) and (b)) or 8 bar (parts (c) and (d)). Orange curves refer to activated catalyst at 240 °C, red curves refer to CO_2 hydrogenation at 240 °C, brown curves refer to CO_2 hydrogenation at 170 °C.

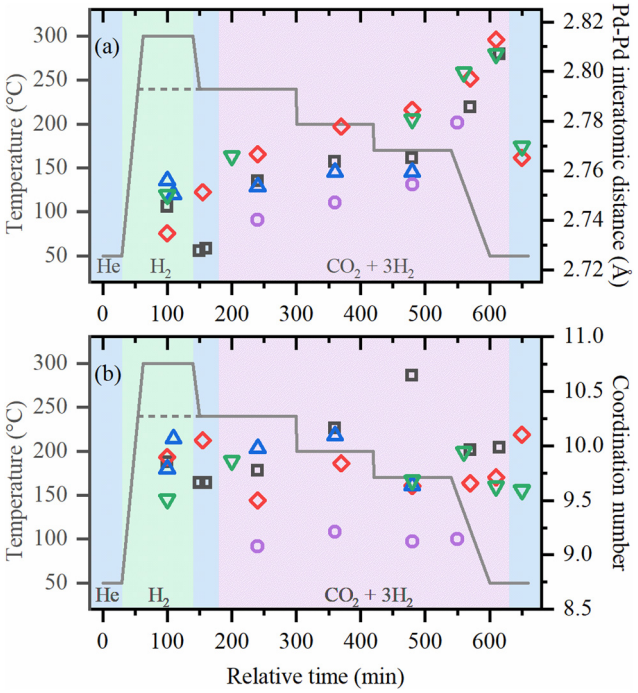

Fig. 3 Pd–Pd interatomic distances (a) and coordination numbers (b) determined by first-shell fitting of EXAFS data collected for the samples activated at 300 °C in H_2 and used for CO_2 hydrogenation under 1 bar and 8 bar (black squares and red diamonds, respectively), activated at 240 °C in H_2 and used for CO_2 hydrogenation under 1 bar and 8 bar (blue up and green down triangles, respectively) and activated directly in reaction mixture at 1 bar at 240 °C (purple circles). Colored areas of the background correspond to different gas environment: blue – helium flow, green – hydrogen flow, pink – reaction mixture.

the first-shell Pd–Pd interatomic distances and the averaged first-shell coordination numbers (Fig. 3, parts (a) and (b), respectively). XANES data (Fig. S2, ESI†) confirm the successful reduction of Pd(II) with formation of Pd NPs, in agreement with our previous reports.[36,37] The coordination numbers in the activated samples were close to 10 irrespective of the activation temperature (240 and 300 °C). The values correspond to the particle size of about 2.6 nm, which is slightly higher than in TEM due to the stronger influence of larger particles in atom-weighted EXAFS signal. Notably, the cell parameter of the UiO-67 framework decreases together with the formation of Pd NPs (Fig. 4). For the sample activated directly in the reaction mixture, lower values of coordination numbers (N = 9) were observed, which can be explained by the stabilization of the small particles due to the interaction with the reagents (*vide infra*).

Under reaction conditions, coordination numbers are stable, but interatomic distances systematically increase for all samples, being larger for lower temperatures and high pressures. After cooling down in the reaction mixture, the values of R_{Pd-Pd} ~ 2.81 Å were observed, which is close to those reported for palladium hydrides.[46–48] However, flushing with helium, performed for the samples investigated at high pressures, results in only partial decrease of R_{Pd-Pd} to *ca.* 2.77 Å which is considerably higher than R_{Pd-Pd} = 2.74 Å expected for metallic palladium, and exceeds the thermal expansion of Pd

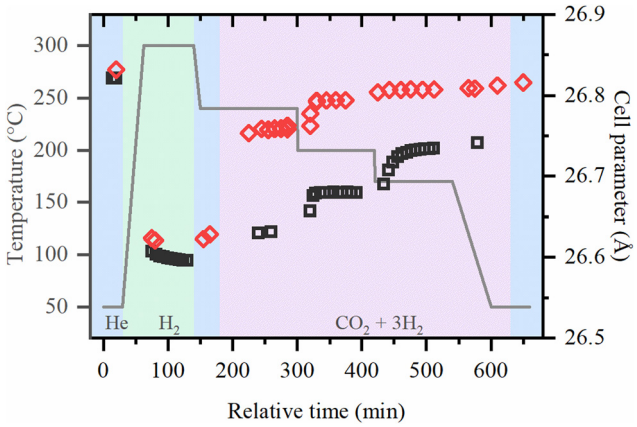

Fig. 4 Cell parameter of UiO-67 samples during activation in H_2 and reaction under 1 bar (black squares) and 8 bar (red diamonds) obtained by the refinement of XRPD data.

NPs.[49] This indicates that apart from palladium hydride, which is known to form reversibly, irreversible formation of an additional phase occurs. For smaller particles formed after activation in the reaction mixture, shorter R_{Pd-Pd} values were observed under reaction conditions. This correlates with the fact that smaller particles have smaller hydrogen (or carbon) storage capacity[50] resulting in a less pronounced cell expansion.

The typical XRPD pattern of UiO-67 (Fig. S3, ESI†) is preserved during both activation procedure and CO_2 hydrogenation reaction, which proves the extreme stability of MOFs with UiO-67 structure. The evolution of the cell parameter is shown in Fig. 4. Under reaction conditions, the cell parameter is increasing with respect to the activated material in pure He and in H_2/He mixture. The increase of the cell parameter is higher at high pressures and lower temperatures, which may indicate the adsorption of reactive molecules inside the pores of UiO-67.

To get further insights into the local structure of Pd sites, we analyzed XANES spectra, which are known to be sensitive to the presence of light atoms, such as H or C, that are not visible in Pd *K*-edge EXAFS.[51–54] Principle component analysis (PCA) analysis revealed the presence of three independent species formed under reaction conditions (Fig. S4 and S5, ESI†). Then, MCR-ALS procedure was applied to represent the whole set of XANES data (Fig. S6, ESI†) by the three representative spectra (Fig. 5a) and their concentration profiles (Fig. 6 and Fig. S7–S9, ESI†). The first component (solid black line) corresponds to the metallic phase of palladium and its concentration is maximal for the fresh samples after activation in H_2. The second component (dotted blue line) is characterized by a shift of the second peak towards smaller energies, due to the increased Pd–Pd distances, characteristic for palladium hydride.[45,50,54] Furthermore, its concentration decreases when after activation in H_2 the sample is flushed with He (Fig. 6 and Fig. S7, ESI†). However, the shape of the first peak is different from that reported for palladium hydrides[46] and is slightly broadened toward higher energies, indicative of Pd–C bonds.[55] Therefore, this component represents the Pd NPs with increased interatomic distances due to the presence of both H and C impurities in the bulk of the particles

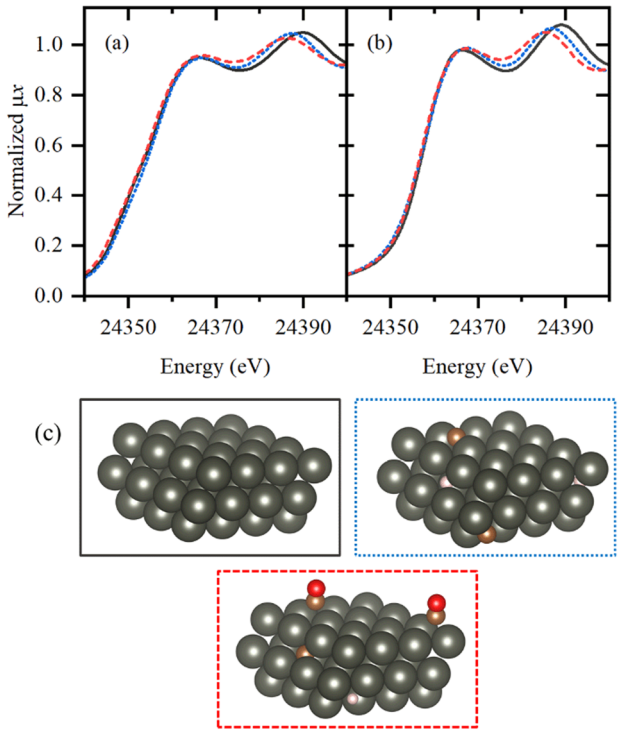

Fig. 5 (a) Pd *K*-edge XANES spectra extracted from the whole experimental dataset by MCR approach. (b) Theoretical spectra calculated for pure Pd surface (solid black), bulk Pd with R_{Pd-Pd} = 2.8426 Å absorbed *ca.* 7% C and *ca.* 7% H atoms (dotted blue) and Pd surface with bridging CO molecule (dashed red). (c) Schematic illustration of atomic structures of palladium surfaces whose simulated XANES spectra reproduces the features observed in (the frame color is the same as for spectra in part (b)). Atoms color code: Pd – dark grey, C – brown, O – red, H – pink MCR components.

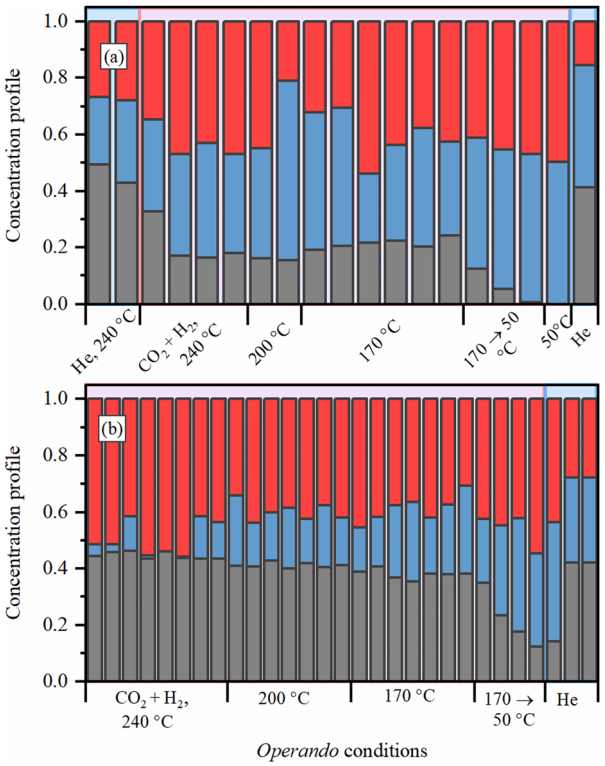

Fig. 6 Evolution of MCR components (the color code is the same as for spectra presented in Fig. 5a) for the samples (a) activated in H_2 at 300 °C and exposed to reaction mixture under 8 bar and (b) activated directly in the reaction mixture under 1 bar at 240 °C.

(Fig. 5c). The last component (dashed red line) is characterized by smaller interatomic distances, but the carbide-like features in the first peak are even more pronounced than in the second component. To reproduce the observed changes, the theoretical spectra were calculated for the structures with CO_2, CO, CH_x, H_2O, O and OH placed on top, bridge or hollow sites (Fig. S10, ESI†) at of palladium surface. The highest similarity with the experimental data was observed in theoretical spectrum for bridge CO configuration, shown in Fig. 5b by dashed red line together with pure Pd surface (solid black). In agreement with the assignment made, the concentration of the last component (surface adsorbed CO) goes to zero after flushing with He, while the second one (bulk carbide) remains stable. Moreover, the separately measured XAS spectra for Pd@γ-Al_2O_3 NPs with a particle size of *ca.* 2.6 nm under CO flow prove the proposed model (Fig. S11, ESI†).

Additional insights into the structure of UiO-67-Pd come from the Zr *K*-edge EXAFS. Due to the complex surroundings of Zr atoms on UiO-67 secondary building units, the fitting of EXAFS data requires a big number of parameters to be taken into consideration. In particular, coordination numbers (N), Debye–Waller factors (σ^2) and interatomic distances (R) for single scattering of two Zr–O, Zr–C and Zr–Zr contributions and Zr–O–O, Zr–O–C and Zr–O–C–O multiple scatterings already require 18 parameters with additional energy corrections (ΔE_0). To reduce the number of independent fitting parameters, only three scattering paths (Zr–O_1, Zr–O_2 and Zr–Zr) were used, where two Zr–O contributions depict the interval 1.2–2.6 Å in *R*-space (phase uncorrected). Furthermore, fitting was performed simultaneously for five EXAFS spectra of the same sample, using shared parameters, and applying several constrains. For instance, interatomic distances for identical paths were used the same for the whole lifespan of the sample, ΔE_0 was fixed at zero, and total coordination number of two oxygen scattering paths was set to 8. Thus, the total number of variable parameters of five EXAFS spectra was 20. The fitting results for the sample activated in H_2 at 300 °C and exposed to reaction mixture under 8 bar for the most essential parameters are summarized in the Table 1.

The Zr–Zr coordination number decreases dramatically upon activation, which is visually seen in Fig. 7, while the increase in the Debye–Waller is consistent with the temperature. Even considering the correlation between these parameters, an additional effect on Zr–Zr coordination beyond thermal disorder is evident. Under reaction conditions, Zr–Zr coordination remains lowered and is only partially restored after cooling down to 50 °C. Therefore, the secondary building units of UiO-67 experience local distortions with a decrease in the coordination of Zr–Zr preserving with the overall stability of the whole UiO-67 framework confirmed by XRPD. FT-EXAFS spectra collected for the sample directly activated in the

Table 1 Fit results of FT-EXAFS for the sample activated in H_2 at 300 °C and exposed to reaction mixture under 8 bar. The fits were performed in the *R*-space over the (1.3–3.8) Å interval on the k^{1-3}-weighted $\chi(k)$ functions Fourier-transformed in the (3.8–14.5) $Å^{-1}$ *k*-space interval. The ΔE_0 was fixed at 0 to all paths. The quality of the fits can be evaluated in Fig. S12 (ESI)

Sample condition/ parameter	As such, room temperature, He flow	After activation at 300 °C, reaction mixture under 8 bar at 240 °C	Reaction mixture under 8 bar at 200 °C	Reaction mixture under 8 bar at 170 °C	After reaction, 50 °C, He flow
$S_0^2 \times N_{Zr-O1}$	2.77 ± 0.25	3.45 ± 0.22	3.29 ± 0.24	3.12 ± 0.22	2.92 ± 0.24
$S_0^2 \times N_{Zr-O2}$	5.23 ± 0.25	4.55 ± 0.22	4.71 ± 0.24	4.88 ± 0.22	5.01 ± 0.24
$S_0^2 \times N_{Zr-Zr}$	4.13 ± 0.07	1.26 ± 0.56	1.88 ± 0.57	2.29 ± 0.57	3.32 ± 0.59
R_{Zr-O1}	2.12 ± 0.03				
R_{Zr-O2}	2.27 ± 0.01				
R_{Zr-Zr}	3.52 ± 0.01				
σ^2_{Zr-O1}	0.003 ± 0.001	0.006 ± 0.001	0.005 ± 0.001	0.005 ± 0.001	0.004 ± 0.001
σ^2_{Zr-O2}	0.004 ± 0.001	0.006 ± 0.001	0.005 ± 0.001	0.005 ± 0.001	0.004 ± 0.001
σ^2_{Zr-Zr}	0.004 ± 0.001	0.006 ± 0.001	0.005 ± 0.001	0.005 ± 0.001	0.004 ± 0.001
R-factor	0.0238	0.0656	0.0413	0.0379	0.0304

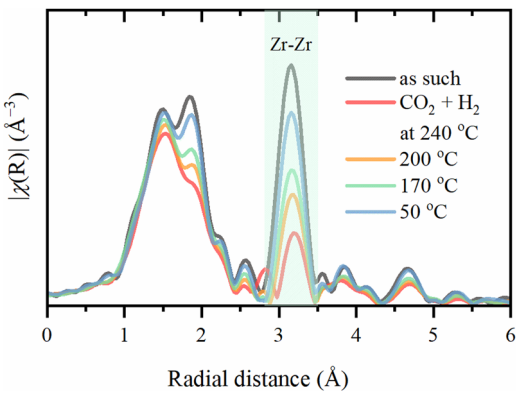

Fig. 7 Experimental phase-uncorrected FT of Zr *K*-edge EXAFS spectra collected for the sample activated in H_2 at 300 °C and exposed to reaction mixture under 8 bar. The highlighted area shows the contribution of Zr–Zr.

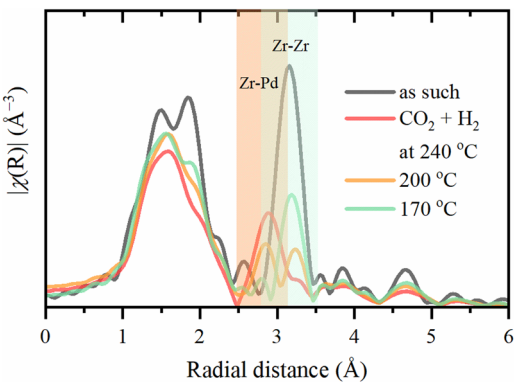

Fig. 8 Experimental phase-uncorrected FT of Zr *K*-edge EXAFS spectra collected for the sample activated directly in the reaction mixture under 1 bar at 240 °C. The orange area shows the contribution of Zr–Pd and the green one – Zr–Zr.

reaction mixture under 1 bar at 240 °C show the appearance of an additional peak at *ca.* 3 Å (Fig. 8), attributed to the Zr–Pd contribution. To elucidate this contribution, we have fitted the EXAFS data at 240 °C using two Zr–O paths and one Zr–Pd path with independent variable parameters. The Zr–Pd path was created by substitution of one Zr atom in UiO-67 inorganic cornerstone by Pd. Addition of the Zr–Zr path does not improve the fit quality as shown in ESI† (Fig. S13). The fit results are summarized in the Table 2.

The CO_2 conversion and product distribution obtained over UiO-67-Pd under conditions mimicking those used during FT-IR and *operando* XAS and XRPD measurements are presented in Fig. 9. The conversion of CO_2 was below 2% under all conditions tested. The catalytic results acquired under FT-IR conditions reveal exclusive formation of CO as the sole product at 1 bar. Conversely, at 8 bar, methanol is detected at all temperatures.

This is in agreement with the fact that formate (Fig. 2), a well-known intermediate of methanol, was only observed at 8 bar using FT-IR. Methane is only observed at 8 bar and 240 °C, which is expected due to the limitation of the kinetics of the Sabatier reaction.[1]

Under XAS/XRPD conditions only CO was observed except at the highest pressure and temperature tested herein, where methane

Table 2 Fit results of FT-EXAFS for the sample directly activated in the reaction mixture under 1 bar at 240 °C. The fits were performed in the *R*-space over the (1.3–3.8) Å interval on the $k^{1,2,3}$-weighted $\chi(k)$ functions Fourier-transformed in the (3.8–14.5) $Å^{-1}$ *k*-space interval. The same ΔE_0 was used for both Zr–O paths

Sample condition/ parameter	Activation and reaction mixture under 1 bar at 240 °C
$S_0^2 \times N_{Zr-O1}$	3.95 ± 8.17
$S_0^2 \times N_{Zr-O2}$	0.97 ± 6.06
$S_0^2 \times N_{Zr-Pd}$	3.90 ± 2.01
R_{Zr-O1}	2.14 ± 0.04
R_{Zr-O2}	2.29 ± 0.04
R_{Zr-Pd}	3.26 ± 0.14
σ^2_{Zr-O1}	0.007 ± 0.018
σ^2_{Zr-O2}	0.002 ± 0.017
σ^2_{Zr-Pd}	0.010 ± 0.003
ΔE_0	−3.61 ± 5.39
ΔE_{Zr-Pd}	−5.45 ± 4.04
R-factor	0.0361

was also formed. The formation of CO, and of methane as a secondary product thereof at high temperature and pressure, is in agreement with literature on Pd nanoparticles in SiO_2 and in UiO-66 MOF.[1,56] To the best of our knowledge, methanol formation

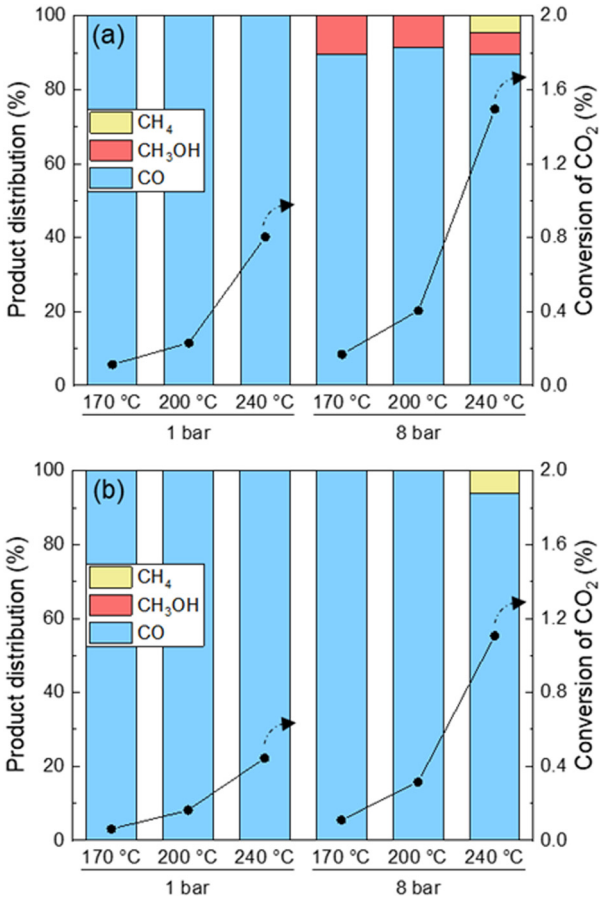

Fig. 9 Product distribution (left axes, bars) and CO_2 conversion (right axes, circles) at 1 and 8 bar and 170, 200 and 240 °C over UiO-67-Pd. CH_4 selectivity (yellow), CH_3OH (red) and CO (blue) and CO_2 conversion (circles). (a) Reduction: 10% H_2 in inert for 4 h at 300 °C. Conditions: H_2/CO_2 = 6/1, contact time (τ) = 0.01 g_{cat} min ml^{-1}. (b) Reduction: 14% H_2 in inert for 0.5 h at 300 °C. Conditions: H_2/CO_2/inert = 3/1/4, contact time (τ) = 0.01 g_{cat} min ml^{-1}.

on Pd–Zr-MOFs is unprecedented in the open literature. However, this observation is well supported by prior studies in which a synergistic interaction between open Zr sites on the $Zr_6O_4(OH)_4$ nodes of UiO-66/-67 and either Pt NPs or Cu NPs has been reported, with the metal NP as the hydrogen activating site, and the metal–Zr interface as the CO_2 activation site. In both cases, formate species attached to the Zr-nodes were identified as intermediates to methanol formation.[35,57–59]

Unfortunately, the overall catalytic performance of Pd NPs embedded in the UiO-67 MOF happened to be quite low for this kind of reaction. Nevertheless, the methodologies developed for the analyses of this material were made available to identify intermediates adsorbed on the surface of the nanoparticles and demonstrated an extreme stability of the Pd-functionalized MOF under reaction conditions.

Materials and methods

Catalyst preparation

The UiO-67-Pd samples were prepared by the following procedure: 135 g of $ZrCl_4$ (1 eq.) was slowly added to a 3L reactor containing 63 ml of distilled water (6 eq.) and 2243 ml of dimethylformamide (DMF) (50 eq.) held at room temperature on a magnetic stirring plate. The solution was heated to 110 °C and 212 g of benzoic acid (3 eq.) was added as a modulator and dissolved rapidly. When the benzoic acid was completely dissolved, 14 g of 2,2′-bipyridine-5,5′-dicarboxylic acid (bpy) was added, followed by 126 g of 1,1′-biphenyl-4,4′-dicarboxylic acid (bpdc). The resulting solution was placed for two days at 120 °C in a jacketed glass reactor (with stirring) equipped with a reflux condenser. The resulting product was isolated by filtration, washed with hot DMF (500 ml) and acetone (1 l) in the filter, and then dried at 150 °C in air overnight. The MOF was then impregnated with $PdCl_2$ (Sigma-Aldrich) in DMF at 100 °C overnight (with stirring).[32] This procedure leads to the formation of well-defined BPYDC-$PdCl_2$ sites. The amount of $PdCl_2$ used for the impregnation corresponded to a 1 : 1 bpy : Pd molar ratio and 4.6 wt% Pd in the final material.

Laboratory characterization

Transmission electron microscopy (TEM) and high-resolution TEM (HR-TEM) measurements were performed using a side entry Jeol JEM 3010 (300 kV) microscope equipped with a LaB_6 filament and fitted with X-ray EDS analysis by a Link ISIS 200 detector. For the analysis, the powdered samples were deposited on a copper grid, coated with a porous carbon film. All digital micrographs were acquired using an Ultrascan 1000 camera and the images were processed by Gatan digital micrograph. A statistically representative number of particles was counted to obtain the Pd particle size distribution with the average value 2.3 nm. The mean particle diameter (d_m) was calculated as follows: $d_m = \Sigma d_i n_i / \Sigma n_i$, where n_i was the number of particles of diameter d_i. Measurements were carried out on UiO-67-Pd after activation at 4 hours at 300 °C in 20 ml (min $0.1 g_{cat})^{-1}$ 10% H_2 in Ar. It is worth noting that the UiO-67-Pd samples proved to be stable to prolonged exposition under the electron beam of the instrument, in terms of UiO-67 crystallinity as well as Pd NPs size (no metal coalescence).

Operando FT-IR technique was performed by means of a Bruker Vertex70 instrument, equipped with a liquid nitrogen-cooled MCT detector. Each spectrum was acquired by averaging 64 acquisitions with a spectral resolution of 2 cm^{-1}. The undiluted sample was pressed to form a pellet of approximately 4 mg and was mounted inside a low free-volume cell from AABSPEC (model #CXX). Such cell allowed pressure, temperature, and gas flow control. The sample was activated at 300 °C (5 °C min^{-1} ramp) in 10% H_2/He (10 ml min^{-1}) for 4 h and then cooled to 240 °C in 10 ml min^{-1} He. Afterwards, the sample was kept under atmospheric pressure and CO_2 hydrogenation (CO_2/H_2 = 1/6, 10 ml min^{-1}, τ = 0.0004 g_{cat} min ml^{-1}) reaction conditions for 2 h. Finally, the temperature was varied to 170 °C, keeping constant the feed composition. Such catalytic test was performed with same temperatures and gas composition, but at 8 bar pressure.

Operando XAS and XRPD

XRPD and Pd *K*-edge XAS data were collected at the BM31 of the ESRF (Grenoble, France). The sample (*ca.* 10 mg) was loaded

inside a 2.5 mm quartz glass capillary and fixed with quartz wool from both sides. The capillary was glued inside a U-shaped sample holder connected to a remotely controlled gas line (see Fig. S14, ESI†). A gas blower was positioned below the sample to control the temperature. The samples were activated *in situ* by heating in a flow of 1.4 ml min^{-1} H_2 and 8.6 ml min^{-1} He from room temperature to 300 °C and left at this temperature for 30 min to allow the formation of nanoparticles. Then, the flow was switched to pure He to remove possible PdH_x phase. The activated material was cooled down to 240 °C, and exposed to a reaction mixture of H_2/CO_2/He = 3/1/4 (7.5, 2.5, and 10 ml min^{-1} of H_2, CO_2, and He, respectively) with a total flow of 20 ml min^{-1} (τ = 0.0005 g_{cat} min ml^{-1}). The reaction was carried out at 240, 200, and 170 °C under a total pressure of 1 and 8 bar, for 2 h under each of the above conditions. The resulting gas mixture after the sample was analyzed by online mass spectrometer (Pfeiffer OmniStar GSD 320).

Pd *K*-edge XAS were obtained in the transmission mode by continuous scanning of the double crystal Si(111) monochromator from 24.1 to 25.3 keV for steady state spectra and during reaction, and from 24.2 to 24.8 keV for measurements during activation. To reduce higher harmonics the monochromator was detuned to 80% of the maximal intensity. The palladium foil was measured simultaneously with each spectrum for energy calibration using a third ionization chamber. For the sample activated at 300 °C at 8 bar and the sample directly activated in reaction mixture, Zr *K*-edge XAS (see Fig. S15, ESI†) were also collected from 17.8 to 19.0 keV alternatively with Pd *K*-edge XAS.

XRPD was measured using 0.51067 Å radiation, selected by a Si(111) channel-cut monochromator. CMOS-Dexela 2D detector covered the 2θ region up to 35°. The values of the photon wavelength, sample to detector distance and detectors tilts have been optimized by Rietveld refinement of NIST LaB_6 and Si samples and kept fixed in the refinement of the Pd/C samples. For better statistics 20 diffraction images and 20 dark images (without X-ray beam) with acquisition time of 5 seconds were collected at each experimental point.

XAS data analysis

Demeter software package[60] was used to process and analyze EXAFS spectra. Background subtraction, normalization and energy calibration were performed in the Athena program using standard parameters. For the Pd *K*-edge, the first shell Fourier analysis of the EXAFS data was performed in the Artemis program using Pd–Pd contribution with four variable parameters: ΔE_0, R_{Pd-Pd}, σ^2_{Pd-Pd}, N_{Pd-Pd}. The fit was performed in *R*-space in 1.0–3.0 Å region for k^2-weighted data Fourier transformed (FT) in 3.0–10.0 $Å^{-1}$ Δk region ($2\Delta k\Delta R/\pi > 8$). The $S_0{}^2$ value was fixed at 0.77 as determined for Pd foil. For the Zr *K*-edge the 4.0–14.0 $Å^{-1}$ Δk and 1.21–3.7 Å ΔR intervals were used for all spectra. One path of Zr–O shell and one path of Zr–Zr were used in the Fourier analysis of the EXAFS data with 8 variable parameters in total.

Analysis of experimental XANES spectra was performed using multivariate curve resolution (MCR) approach implemented in pyMCR 0.3.1.[61] The whole dataset of normalized experimental spectra was represented by matrix D of size $m \times n$, where m is the number of spectra and n is the number of energy points. This matrix is decomposed as $D = CS^T + E$, where C with size $m \times k$ is the concentration profiles of k pure components from matrix S ($n \times k$), and E ($m \times n$) is the error matrix. The energy ranges were limited to 24.33–24.41 keV. The optimal number of components was determined from the PCA implemented in PyFitIt.[62–64]

Theoretical XANES calculation

Theoretical XANES spectra were calculated within a full potential finite difference method of FDMNES code.[65,66] The computational sphere radius was chosen as 5.2 Å. The surfaces were represented by unit cell with 32 Pd atoms, adsorbed species (CO_2, CO, CH_3, H_2O, O and OH placed on top, bridge, or hollow sites) and 13 Å of vacuum (see Fig. S10, ESI†). All geometries were initially optimized in VASP 5.3 code[67–69] with PBE exchange–correlation potential using a 8 × 4 × 1 Monkhorst Pack grid with the plane-wave basis cutoff at 500 eV.

XRPD data analysis

2D XRPD images were averaged in PyFAI code[70] to obtain $I(2\theta)$ patterns. Whole-pattern fitting by Pawley method was performed in Jana2006 code.[71] The used 2θ-range was from 3 to 30°. The initial structure was based on a cubic cell of UiO-67 in $Fm\bar{3}m$ symmetry with cell parameter a = 26.8 Å. The variable parameters included cell parameter (a), three parameters of Pseudo-Voight function and ten parameters of the background function.

Catalytic testing

Catalytic tests were performed under conditions mimicking those used in XAS/XRPD and FT-IR studies, using a commercial Microactivity Effi reactor (PID Eng & Tech) with a fixed bed flow setup. The reactor is a stainless-steel reactor (I.D. 6 mm) coated with silicon, connected to an Agilent 8890 gas chromatogram (GC) equipped with two flame ionization detectors (FIDs) and a thermal conductivity detector (TCD). One of the FIDs was coupled to a methanizer to achieve lower detection limits of CO and CO_2. The Pd-UiO-67 sample was tested under two different conditions to better compare the activity of the material under similar conditions to those during XAS and FT-IR characterization. To imitate the conditions during XAS and XRPD, 0.2 g catalyst were reduced in 14% H_2 in inert for 0.5 h at 300 °C. The catalyst was tested at 240, 200 and 170 °C at 1 and 8 bar for 4 h under a reaction mixture of H_2/CO_2/Inert = 3/1/4 with a total flow of 20 ml min^{-1} (τ = 0.01 g_{cat} min ml^{-1}). To replicate the condition used during FT-IR spectroscopy, 0.2 g UiO-67-Pd was reduced in 10% H_2 in inert for 4 h at 300 °C before being exposed to a reaction mixture of H_2/CO_2 = 6/1 with a total flow of 20 ml min^{-1} (τ = 0.01 g_{cat} min ml^{-1}). The catalyst was tested at 240, 200 and 170 °C at 1 and 8 bar.

Conclusions

Summarizing the *operando* study on UiO-67-Pd MOF, we can conclude that: (i) under reaction conditions, mixed palladium

hydride and carbide phases are formed; (ii) the hydride phase is stronger at high pressure and low temperatures, but is removed upon flushing in He, while the carbide one is stable even after flushing; (iii) formation of CO adsorbed species is observed under reaction conditions, and can act as stabilizing factor for smaller Pd NPs formed upon activation directly in the reaction mixture; (iv) Zr–O coordination in the inorganic building units of UiO-67 is reduced during CO_2 hydrogenation reaction that is the more considerable at the higher temperature, while the overall UiO-67 lattice remains stable under all conditions; (v) a Zr/Pd interface is observed in EXAFS, being responsible for methanol formation in UiO-67-Pd samples.

Author contributions

ALB, EGK, AAS, AL, DKS, and CA-S carried out experiments, performed data analysis and theoretical calculations. ALB, AL and UO designed the experiments. AAS and ALB wrote the original draft of the manuscript. ALB, SB and UO: manuscript revising and funding acquisition. All authors discussed and contributed to the work.

Conflicts of interest

There are no conflicts to declare.

Acknowledgements

CA-S, AL, DKS, SB and UO acknowledge the Research Council of Norway for financial support of this research through contracts no. 250795 (CONFINE) and 288331 (CO2LO). Dr Gurpreet Kaur is acknowledged for the synthesis of UiO-67-Pd. We thank ESRF for providing the beamtime and Dragos Stoian and Wouter van Beek for their support during experiment at BM31 beamline. We acknowledge ALBA for the additional measurements on commercial Pd NPs under CO atmosphere.

References

1 J. Martins, N. Batail, S. Silva, S. Rafik-Clement, A. Karelovic, D. P. Debecker, A. Chaumonnot and D. Uzio, *Catal. Commun.*, 2015, **58**, 11–15.
2 S. Kattel, P. J. Ramírez, J. G. Chen, J. A. Rodriguez and P. Liu, *Science*, 2017, **355**, 1296–1299.
3 H. Bahruji, M. Bowker, G. Hutchings, N. Dimitratos, P. Wells, E. Gibson, W. Jones, C. Brookes, D. Morgan and G. Lalev, *J. Catal.*, 2016, **343**, 133–146.
4 A. Ota, E. L. Kunkes, I. Kasatkin, E. Groppo, D. Ferri, B. Poceiro, R. M. Navarro Yerga and M. Behrens, *J. Catal.*, 2012, **293**, 27–38.
5 N. Koizumi, X. Jiang, J. Kugai and C. Song, *Catal. Today*, 2012, **194**, 16–24.
6 L. Zhang, Y. Zhang and S. Chen, *Appl. Catal., A*, 2012, **415–416**, 118–123.
7 A. Ramirez, *et al.*, *JACS Au*, 2021, **1**(10), 1719–1732.
8 R. Raudaskoski, M. V. Niemelä and R. L. Keiski, *Top. Catal.*, 2007, **45**, 57–60.
9 A. Prašnikar, A. Pavlišič, F. Ruiz-Zepeda, J. Kovač and B. Likozar, *Ind. Eng. Chem. Res.*, 2019, **58**, 13021–13029.
10 N. Rui, Z. Wang, K. Sun, J. Ye, Q. Ge and C.-J. Liu, *Appl. Catal., B*, 2017, **218**, 488–497.
11 A. A. Skorynina, *et al.*, *Radiat. Phys. Chem.*, 2020, **175**, 108079.
12 W. Stuyck, *et al.*, *J. Catal.*, 2022, **408**, 88–97.
13 V. V. Butova, M. A. Soldatov, A. A. Guda, K. A. Lomachenko and C. Lamberti, *Russ. Chem. Rev.*, 2016, **85**, 280–307.
14 T. A. Goetjen, J. Liu, Y. Wu, J. Sui, X. Zhang, J. T. Hupp and O. K. Farha, *Chem. Commun.*, 2020, **56**, 10409–10418.
15 A. Yu. Pnevskaya, *et al.*, *J. Phys. Chem. C*, 2021, **125**(40), 22295–22300.
16 A. Yu. Pnevskaya and A. L. Bugaev, *Results Chem.*, 2023, **5**, 100831.
17 D. Ma, B. Li, K. Liu, X. Zhang, W. Zou, Y. Yang, G. Li, Z. Shi and S. Feng, *J. Mater. Chem. A*, 2015, **3**, 23136–23142.
18 L. Wang, P. Jin, S. Duan, J. Huang, H. She, Q. Wang and T. An, *Environ. Sci.: Nano*, 2019, **6**, 2652–2661.
19 Y. Dou, H. Zhang, A. Zhou, F. Yang, L. Shu, Y. She and J.-R. Li, *Ind. Eng. Chem. Res.*, 2018, **57**, 8388–8395.
20 B. Gole, U. Sanyal, R. Banerjee and P. S. Mukherjee, *Inorg. Chem.*, 2016, **55**, 2345–2354.
21 A. A. Tereshchenko, *et al.*, *Inorg. Chem.*, 2022, **61**(9), 3875–3885.
22 W. Dong, C. Feng, L. Zhang, N. Shang, S. Gao, C. Wang and Z. Wang, *Catal. Lett.*, 2015, **146**, 117–125.
23 J. H. Cavka, S. Jakobsen, U. Olsbye, N. Guillou, C. Lamberti, S. Bordiga and K. P. Lillerud, *J. Am. Chem. Soc.*, 2008, **130**, 13850–13851.
24 K. S. Vetlitsyna-Novikova, V. V. Butova, I. A. Pankin, V. V. Shapovalov and A. V. Soldatov, *J. Surf. Invest.: X-Ray, Synchrotron Neutron Tech.*, 2019, **13**, 787–792.
25 V. V. Butova, O. A. Burachevskaya, I. V. Ozhogin, G. S. Borodkin, A. G. Starikov, S. Bordiga, A. Damin, K. P. Lillerud and A. V. Soldatov, *Microporous Mesoporous Mater.*, 2020, **305**, 110324.
26 V. V. Butova, K. S. Vetlitsyna-Novikova, I. A. Pankin and A. V. Soldatov, *J. Surf. Invest.: X-Ray, Synchrotron Neutron Tech.*, 2020, **14**, 318–323.
27 K. E. deKrafft, W. S. Boyle, L. M. Burk, O. Z. Zhou and W. Lin, *J. Mater. Chem.*, 2012, **22**, 18139–18144.
28 R. Dalapati, B. Sakthivel, A. Dhakshinamoorthy, A. Buragohain, A. Bhunia, C. Janiak and S. Biswas, *CrystEngComm*, 2016, **18**, 7855–7864.
29 E. Borfecchia, S. Øien, S. Svelle, L. Mino, L. Braglia, G. Agostini, E. Gallo, K. A. Lomachenko, S. Bordiga, A. A. Guda, M. A. Soldatov, A. V. Soldatov, U. Olsbye, K. P. Lillerud and C. Lamberti, *J. Phys.: Conf. Ser.*, 2016, **712**, 012125.
30 L. Braglia, E. Borfecchia, K. A. Lomachenko, A. L. Bugaev, A. A. Guda, A. V. Soldatov, B. T. L. Bleken, S. Øien-Ødegaard, U. Olsbye, K. P. Lillerud, S. Bordiga, G. Agostini, M. Manzoli and C. Lamberti, *Faraday Discuss.*, 2017, **201**, 265–286.
31 L. Braglia, E. Borfecchia, L. Maddalena, S. Øien, K. A. Lomachenko, A. L. Bugaev, S. Bordiga, A. V. Soldatov,

K. P. Lillerud and C. Lamberti, *Catal. Today*, 2017, **283**, 89–103.
32 A. L. Bugaev, A. A. Guda, K. A. Lomachenko, E. G. Kamyshova, M. A. Soldatov, G. Kaur, S. Øien-Ødegaard, L. Braglia, A. Lazzarini, M. Manzoli, S. Bordiga, U. Olsbye, K. P. Lillerud, A. V. Soldatov and C. Lamberti, *Faraday Discuss.*, 2018, **208**, 287–306.
33 C. Wang, A. Wang, Z. Yu, Y. Wang, Z. Sun, V. M. Kogan and Y.-Y. Liu, *Catal. Commun.*, 2021, **148**, 106178.
34 E. S. Gutterød, S. Øien-Ødegaard, K. Bossers, A.-E. Nieuwelink, M. Manzoli, L. Braglia, A. Lazzarini, E. Borfecchia, S. Ahmadigoltapeh, B. Bouchevreau, B. T. Lønstad-Bleken, R. Henry, C. Lamberti, S. Bordiga, B. M. Weckhuysen, K. P. Lillerud and U. Olsbye, *Ind. Eng. Chem. Res.*, 2017, **56**, 13206–13218.
35 E. S. Gutterod, A. Lazzarini, T. Fjermestad, G. Kaur, M. Manzoli, S. Bordiga, S. Svelle, K. P. Lillerud, E. Skulason, S. Oien-Odegaard, A. Nova and U. Olsbye, *J. Am. Chem. Soc.*, 2020, **142**, 999–1009.
36 A. L. Bugaev, A. A. Skorynina, L. Braglia, K. A. Lomachenko, A. Guda, A. Lazzarini, S. Bordiga, U. Olsbye, K. P. Lillerud, A. V. Soldatov and C. Lamberti, *Catal. Today*, 2019, **336**, 33–39.
37 E. G. Kamyshova, A. A. Skorynina, A. L. Bugaev, C. Lamberti and A. V. Soldatov, *Radiat. Phys. Chem.*, 2020, **175**, 108144.
38 O.A. Usoltsev, *et al.*, *Nanomaterials*, 2020, **10**(9), 1643.
39 J. Jaumot, R. Gargallo, A. de Juan and R. Tauler, *Chemom. Intell. Lab. Syst.*, 2005, **76**, 101–110.
40 R. Tauler, *Chemom. Intell. Lab. Syst.*, 1995, **30**, 133–146.
41 J. Jaumot, A. de Juan and R. Tauler, *Chemom. Intell. Lab. Syst.*, 2015, **140**, 1–12.
42 D. Yang, M. A. Ortuno, V. Bernales, C. J. Cramer, L. Gagliardi and B. C. Gates, *J. Am. Chem. Soc.*, 2018, **140**, 3751–3759.
43 A. Lazzarini, E. Groppo, G. Agostini, E. Borfecchia, F. Giannici, G. Portale, A. Longo, R. Pellegrini and C. Lamberti, *Catal. Today*, 2017, **283**, 144–150.
44 E. Groppo, W. Liu, O. Zavorotynska, G. Agostini, G. Spoto, S. Bordiga, C. Lamberti and A. Zecchina, *Chem. Mater.*, 2010, **22**, 2297–2308.
45 O. Usoltsev, *et al.*, *Small Methods*, 2024, 2301397.
46 A. L. Bugaev, A. A. Guda, K. A. Lomachenko, A. Lazzarini, V. V. Srabionyan, J. G. Vitillo, A. Piovano, E. Groppo, L. A. Bugaev, A. V. Soldatov, V. P. Dmitriev, R. Pellegrini, J. A. van Bokhoven and C. Lamberti, *J. Phys.: Conf. Ser.*, 2016, **712**, 012032.
47 A. L. Bugaev, A. A. Guda, K. A. Lomachenko, V. V. Shapovalov, A. Lazzarini, J. G. Vitillo, L. A. Bugaev, E. Groppo, R. Pellegrini, A. V. Soldatov, J. A. van Bokhoven and C. Lamberti, *J. Phys. Chem. C*, 2017, **121**, 18202–18213.
48 Aram L. Bugaev, O. A. Usoltsev, A. Lazzarini, K. A. Lomachenko, A. A. Guda, R. Pellegrini, M. Carosso, J. G. Vitillo, E. Groppo, J. A. van Bokhoven, A. V. Soldatov and C. Lamberti, *Faraday Discuss.*, 2018, **208**, 187–205.
49 O. A. Usoltsev, A. A. Skorynina, B. O. Protsenko, V. Martin-Diaconescu, R. Pellegrini, A. V. Soldatov, J. van Bokhoven and A. L. Bugaev, *Appl. Surf. Sci.*, 2023, **614**, 156171.
50 W. Liu, *et al.*, *J. Mater. Chem. A*, 2021, **9**(16), 10354–10363.
51 A. L. Bugaev, A. A. Guda, I. A. Pankin, E. Groppo, R. Pellegrini, A. Longo, A. V. Soldatov and C. Lamberti, *Catal. Today*, 2019, **336**, 40–44.
52 A. L. Bugaev, V. V. Srabionyan, A. V. Soldatov, L. A. Bugaev and J. A. V. Bokhoven, *J. Phys.: Conf. Ser.*, 2013, **430**, 012028.
53 O. A. Usoltsev, *et al.*, *Topics in Catalysis*, 2020, **63**, 58–65.
54 O. A. Usoltsev, *et al.*, *J. Phys. Chem. C*, 2022, **126**(10), 4921–4928.
55 A. L. Bugaev, A. A. Guda, A. Lazzarini, K. A. Lomachenko, E. Groppo, R. Pellegrini, A. Piovano, H. Emerich, A. V. Soldatov, L. A. Bugaev, V. P. Dmitriev, J. A. van Bokhoven and C. Lamberti, *Catal. Today*, 2017, **283**, 119–126.
56 H. Jiang, Q. Gao, S. Wang, Y. Chen and M. Zhang, *J. CO2 Util.*, 2019, **31**, 167–172.
57 B. Rungtaweevoranit, J. Baek, J. R. Araujo, B. S. Archanjo, K. M. Choi, O. M. Yaghi and G. A. Somorjai, *Nano Lett.*, 2016, **16**, 7645–7649.
58 Y. Zhu, J. Zheng, J. Ye, Y. Cui, K. Koh, L. Kovarik, D. M. Camaioni, J. L. Fulton, D. G. Truhlar and M. Neurock, *Nat. Commun.*, 2020, **11**, 5849.
59 E. S. Gutterød, S. H. Pulumati, G. Kaur, A. Lazzarini, B. G. Solemsli, A. E. Gunnæs, C. Ahoba-Sam, M. E. Kalyva, J. A. Sannes and S. Svelle, *J. Am. Chem. Soc.*, 2020, **142**, 17105–17118.
60 B. Ravel and M. Newville, *J. Synchrotron Radiat.*, 2005, **12**, 537–541.
61 C. H. Camp Jr., *J. Res. Natl. Inst. Stand. Technol.*, 2019, **124**, 1–10.
62 A. Martini, A. A. Guda, S. A. Guda, A. L. Bugaev, O. V. Safonova and A. V. Soldatov, *Phys. Chem. Chem. Phys.*, 2021, **23**, 17873–17887.
63 A. Martini, A. A. Guda, S. A. Guda, A. Dulina, F. Tavani, P. D'Angelo, E. Borfecchia and A. V. Soldatov, Cham, 2021.
64 A. Martini, S. A. Guda, A. A. Guda, G. Smolentsev, A. Algasov, O. Usoltsev, M. A. Soldatov, A. Bugaev, Y. Rusalev, C. Lamberti and A. V. Soldatov, *Comput. Phys. Commun.*, 2020, **250**, 107064.
65 A. A. Guda, S. A. Guda, M. A. Soldatov, K. A. Lomachenko, A. L. Bugaev, C. Lamberti, W. Gawelda, C. Bressler, G. Smolentsev, A. V. Soldatov and Y. Joly, *J. Phys.: Conf. Ser.*, 2016, **712**, 012004.
66 S. A. Guda, A. A. Guda, M. A. Soldatov, K. A. Lomachenko, A. L. Bugaev, C. Lamberti, W. Gawelda, C. Bressler, G. Smolentsev, A. V. Soldatov and Y. Joly, *J. Chem. Theory Comput.*, 2015, **11**, 4512–4521.
67 G. Kresse and J. Furthmüller, *Phys. Rev. B: Condens. Matter Mater. Phys.*, 1996, **54**, 11169–11186.
68 G. Kresse and D. Joubert, *Phys. Rev. B: Condens. Matter Mater. Phys.*, 1999, **59**, 1758–1775.
69 J. Hafner, *J. Comput. Chem.*, 2008, **29**, 2044–2078.
70 J. Kieffer and J. P. Wright, *Powder Diffr.*, 2013, **28**, S339–S350.
71 V. Petříček, M. Dušek and L. Palatinus, *Z. Kristallogr. - Cryst. Mater.*, 2014, **229**, 345–352.

